Corrosion Science 209 (2022) 110777

Contents lists available at ScienceDirect

Corrosion Science

journal homepage: www.elsevier.com/locate/corsci

Effects of the heat treatment on the microstructure and corrosion behavior of 316 L stainless steel manufactured by Laser Powder Bed Fusion

J. Bedmar [a], S. García-Rodríguez [a,*], M. Roldán [b], B. Torres [a], J. Rams [a]

[a] Área de Ciencia e Ingeniería de Materiales, ESCET, Universidad Rey Juan CarlosC/ Tulipán s/n, Móstoles, 28933 Madrid, Spain
[b] CIEMAT, National Fusion Laboratory, Technology Division, Avda. Complutense, 40, 28040 Madrid, Spain

ARTICLE INFO

Keywords:
Stainless steel
SEM
EIS
Polarization
Laser Powder Bed Fusion
Heat treatment

ABSTRACT

Additively manufactured AISI 316 L stainless steel samples were heat treated at temperatures from 400 °C to 1100 °C, and the corrosion behavior in chloride environments was electrochemically studied. Heat treatments at 400 °C and 650 °C increased the grain size and the treatment at 1100 °C formed $MnCr_2O_4$ inclusions. Also, these postprocessing techniques reduce the hardness and increased the porosity. Heat treatment at 400 °C increased the polarization resistance and maintained the pitting corrosion mechanisms of the additively manufactured samples. Heat treatments at higher temperatures reduced the polarization resistance but changed the corrosion resistance mechanisms.

1. Introduction

Additive Manufacturing (AM) is a set of new techniques based on the fabrication of parts layer by layer from an STL archive without the needing for expensive tools like molds. One promising AM technique is the Laser Powder Bed Fusion (LPBF), also known as Selective Laser Melting (SLM), which consists of the melting by laser of metal powder after its deposition in a powder bed with the help of a protective atmosphere [1], like Argon. This technique can fabricate near-net-shape parts with complex geometries at no additional costs [2]. This allows a big personalization of the fabricated parts, making this technique ideal for unique pieces for different areas like the aerospace industry [3], the biomedical sector [4], or jewelry [5].

The LPBF process can cause several negative effects on the mechanical properties like the ductility [1] caused by different defects like anisotropy [6], residual stress [7], porosity [8] and lacks of fusion [9]. Anisotropy is associated with several causes from the scan strategy to the different directions of the grains which grow during the solidification [10] or the multiple oxides that can be formed between layers [11]. On the other hand, the residual stress is caused by multiple processes of melting, remelting, reheating, and fast cooling, and the phase changes that occur during the printing process [12]. Finally, defects of voids can be caused by different reasons: porosity appears as gas that gets entrapped during the solidification process, while lack of fusion appears due to suboptimal energy input in the fabrication [13]. Therefore, it has been studied that these problems are linked, for example, the porosity can worsen the anisotropy of the material [14].

Besides the defects, other problems have been investigated, like the layer structure and the rotation angle of the AM parts, which can have different effects on the mechanical properties [15] and the corrosion resistance [16]; the surface roughness which has negative effects in the fatigue properties [17] or the metastable phases which also worse mechanical properties like ductility [18] and the electrochemical behavior [19].

To reduce the mentioned problems, several postprocessing techniques are required to improve the properties of the AM parts. In this way, Laser Shock Peening has been proved to be a good technique to improve the fatigue life of the material [20]; Hot Isostatic Pressing can reduce the number of cracks and pores [21], or electropulsing can modify the microstructure of the LPBF parts or improve their ductility [22].

One of the most used post-processes is the heat treatment in all the ranges it can work. It has been demonstrated in different works that the heat treatment can homogenize the structure, which can improve the hardness and relieve the residual stress of the fabricated parts [23]. On the other hand, also these heat treatments can decrease properties like the yield strength [24], they can improve the ductility, and reduce almost all the anisotropy except the one caused by the presence of pores [25].

Although heat treatments are necessary to improve different

* Corresponding author.
E-mail address: sonia.garcia@urjc.es (S. García-Rodríguez).

https://doi.org/10.1016/j.corsci.2022.110777
Received 1 February 2022; Received in revised form 15 September 2022; Accepted 20 October 2022
Available online 21 October 2022

properties of the AM parts and reduce the defects caused during the fabrication, it is necessary to evaluate the corrosion behavior of the specimens after the post-processing, as is done in this study with 316 L stainless steel parts.

316 L stainless steel is one of the most used materials in the additive manufacturing of metals. This austenitic steel is known for its good mechanical properties and corrosion resistance [26]. A big range of its properties has been studied and it has been demonstrated that its mechanical properties are even higher than those fabricated by conventional processes [27]. On the other hand, higher corrosion resistance of the 316 L stainless steel has been found due to the microstructure caused by the LPBF technique [28]. However, the previously mentioned defects are still in this AM metal, like anisotropy [29], residual stress [30], or porosity [31] are still in this material, so the necessity of a post-processing method like the heat treatment is still necessary, as shown in the work of M. Laleh et al. [32], although not of all these defects imply a detrimental in all the properties. For example, it has been claimed that the presence of porosity does not worsen the bending properties [33] or residual stress does not have negative effects on the pitting susceptibility [34].

Related to the corrosion resistance of the 316 L stainless steel fabricated by LPBF, several studies claim that the as-built parts have excellent corrosion resistance, presenting specially a good pitting corrosion resistance [35] due to the absence of MnS inclusions and the good homogeneity of the composition of chromium [36,37]. However, other studies claim that the presence of pores in the microstructure induces pitting mechanisms [36] and that this mechanism has a metastable behavior [37] but these mechanisms are still unclear. It has been considered that the processes that control the pitting corrosion are associated with the environmental aggressiveness of the chloride media used [38]. It has also been proposed that the presence of residual stress may contribute to the corrosion mechanism of the AM 316 L samples [39], which can be controlled by performing heat treatments at temperatures above 900 °C [40]. However, these processes may induce the formation of new phases that may promote the appearance of new corrosion mechanisms. Therefore, it is necessary to study how the postprocessing techniques that are used to reduce the microstructural defects and control the residual stress influence the corrosion behavior. Also, the effect of heat treatments at temperatures below those commonly used in conventionally manufactured stainless steels has not been studied, despite the different responses of AM 316 L to heat treatments.

In this work, a deep study of the influence of a big range of heat treatment temperatures, from 400 °C to 1100 °C, on the corrosion properties has been done to prove how the elimination of intrinsic characteristics of the LPBF 316 L stainless steel, like anisotropy, residual stress, or porosity, influence one of the most relevant properties of this metal, which is the corrosion resistance. The progress of the knowledge in how the heat treatment temperature influences the formation of a corrosion products layer, and the corrosion performance of the 316 L stainless steel fabricated by LPBF made in this study allows a good selection of these methods to reduce the defects and improve the mechanical properties without worsening the corrosion behavior.

2. Materials and methods

2.1. Materials and process parameters

The AISI 316 L stainless steel powder used was supplied by LPW Technology and had a nominal composition in %wt. of: chromium (16−18), nickel (10−14), molybdenum (2−3), manganese (≤ 2), silicon (≤ 1), nitrogen (≤ 0,1), oxygen (≤ 0,1), phosphorus (≤ 0045), carbon (≤ 0,03), sulfur (≤ 0,03) and iron (rest).

The samples were manufactured with a Laser Powder Bed Fusion system equipped with a fiber laser (EOS M280 400 W). The laser beam used for the fabrication had a wavelength of 1070 nm, a Gaussian shape, and a power of 195 W, the laser spot had a diameter of 0.07 mm. The scanning speed of the process was 1083 mm/s, the laser height was 20 μm and the hatching was 90 μm. The parts were built with the orientation shown in Fig. 1.

The printed parts were ground with SiC emery paper up to 1200 grade and post-processed by the three different heat treatments shown in Table 1.

2.2. Microstructural characterization

The microstructural analysis of the as-built and the heat-treated parts was carried out by optical microscopy (Leica DMR equipped with Leica Image Pro-Plus software) and Scanning Electron Microscopy (SEM) with an accelerating voltage of 15 kV using a Hitachi S-3400 N microscope equipped with an Energy Dispersive X-Ray Spectrometer (EDS, Bruker AXS Xflash Detector 5010). For this study, the as-built and heat-treated parts were cut and embedded, mechanically polished, and electroetched in 10% oxalic acid solution at a potential of 6 V.

Porosity was measured by optical microscopy, measuring 10 different zones per part by using the Leica Image Pro-plus software to obtain the percentage of porosity in every zone.

Archimedes' density method was used to measure the influence of the heat treatment on the density of the studied parts, comparing the results with those obtained by analyzing the porosity by optical microscopy. Every part was weight in the air and immersed in water and the Archimedes density, ρ, was obtained by the Eq. 1:

$$\rho = \frac{W(a)\quad[\rho(fl) - \quad\rho(a)]}{[W(a) - W(fl)]} + \quad \rho(a) \tag{1}$$

Where $W(a)$ is the weight of the part measured in the air; $\rho(fl)$, the density of the water in which the part is immersed counting with its temperature; $\rho(a)$, the air density in room conditions; and $W(fl)$, the weight of the part immersed in water.

Grain size, G, was measured to study the influence of the heat treatments on it. G was obtained by using Eq. 2:

$$N' \quad = 2^{(G+3)} \tag{2}$$

Where N' is the number of grains per mm^2 counted in a zone. Five measurements were taken to ensure the quality of the measurements. In conclusion, an increment of the G parameter indicates a decrease in the grain size.

X-ray diffraction (XRD) using a Philips X'Pert diffractometer (CuKα=1.54056 Å) was used to identify the phases formed in the samples.

The microstructures of the Alloys have been characterized on thin foils using transmission electron microscopy (TEM) and scanning TEM (STEM) techniques on a JEOL JEM 3000 F equipped with an EDS detector and field emission Schottky gun, with an accelerating voltage of

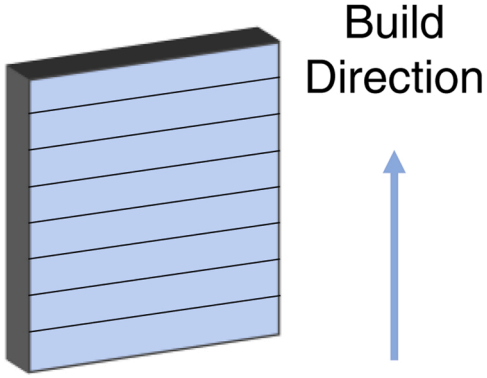

Fig. 1. Build orientation of the manufactured parts.

Table 1
Heat treatments conditions.

Sample	Temperature (°C)	Treatment time (h)	Cooling method
as-SS/SLM	None	None	None
SS/SLM/400	400	4	Annealing
SS/SLM/650	650	2	Annealing
SS/SLM/1100	1100	0.5	Tempering

300 kV. The STEM unit has an annular dark field detector (ADF) that makes it possible to acquire both, low angle (LAADF) and high angle annular dark field (HAADF) images by changing the camera length. The characterization of microstructure has been mainly performed in STEM mode by acquiring LAADF images or in some cases- HAADF images to remove contrast from forest dislocations and to obtain a purer Z-contrast of the precipitates in the images.TEM discs with 3 mm in diameter were thinned using a Struers Tenupol-5 electropolishing unit in a solution of 10% perchloric acid and 90% acetic at 10 V and 15 °C. Microchemical analysis performed by EDX Oxford INCA on secondary phases was carried out on the same thin foils.

Microhardness tests were carried out using a Microhardness Tester (SHIMADZU HMV-2TE) by applying loads of 980.7 mN (HV0.1) for 15 s on the polished samples with a Vickers penetrator. The average hardness value was calculated after ten indentations.

2.3. Electrochemical testing

Electrochemical tests of the several parts were carried out using a three-electrode cell configuration: the working electrode, which was the analyzed sample; a reference electrode of silver/silver chloride (Ag/AgCl, KCl 3 M), and a counter electrode of graphite. These tests were performed in a 3.5% NaCl water and aerated stagnant solution at controlled room temperature with an Autolab PGStat302N potentiostat, provided with Nova 2.1 software. The surface of each sample was ground up to 1200 before the tests.

Linear polarization tests were carried out for 168 h of immersion varying the potential from ± 10 mV around the corrosion potential (*Ecorr*) and using a scanning rate of 1 mV/s to calculate the Polarization Resistance (R_p) of the specimens. *Rp* values were obtained by triplicate at different time lengths: 1, 6, 24, 48, 72, 96, and 168 h to study the evolution of this parameter through time.

Tafel tests (anodic – cathodic polarization measurements) were performed by polarizing the samples between −800 mV and 1 V around the *Ecorr* with a scanning rate of 1 mV/s. Three tests were made for each condition in different specimens after 1 h of immersion.

Cyclic potentiodynamic tests were carried out to determine the susceptibility to localized corrosion. A polarization scan was carried out in the anodic direction, starting at − 1.4 V, at a rate of 0.1 V/s with a maximum and minimum potential of 1 V and −1.4 V, respectively, around the Ecorr. The sweep direction was reversed at a limit threshold of 5 mA/cm^2. These tests were performed after 1 h of immersion by triplicate in different samples.

EIS tests were performed at the same times as the Polarization Resistances tests. These AC Electrochemical Impedance tests were performed by a sinusoidal potential wave at *Ecorr* with an amplitude of 10 mV over the frequency range from 10^5 to 10^{-2} Hz, recording 10 points per decade, resulting in Nyquist and Bode plots. The fitting of the curves to determine the equivalent circuits was made with the FRA software from Autolab and the best fitting values are shown for each test. The accuracy of the fitting values was not included because of the variability of experimental and fitting errors.

3. Results and discussion

3.1. Effect of heat treatment on phase and microstructure

Fig. 2 shows the XRD patterns obtained for the as-SS/SLM specimen and the heat-treated samples. The only peak that appears in the XRD spectra of the as-manufactured samples was austenite, and no additional peaks of any new phase were observed on the heat-treated samples. However, the limited sensitivity of XRD phase analysis does not allow observing the formation of other minor phases besides austenite. So, the formation of other minor phases caused by the heat treatments, like delta or sigma ferrite or some intermetallic phases, cannot be excluded.

The LPBF stainless steel sample has a macroscale structure as shown in Fig. 3. The micrography, in the plane parallel to the building platform, reveals a structure that is determined by the laser-scanning pattern and is characterized by the molten and rapidly solidified regions. The structure of the planes perpendicular to the building platform shows that the manufacturing process, due to the overlap of the laser-scanning pattern, leads to the formation of a network of melt pools.

SEM micrographs of the different samples are shown in Figs. 4 and 5. The as-SS/SLM specimen showed a complex cellular microstructure and fine sub-grains characteristic of the LPBF processed samples. The high density of the microstructure is demonstrated as it has very few spherical pores.

In Fig. 4a and Fig. 5a, it can be seen the general microstructure of an as-built SS 316 L specimen. At low magnification, melt pools can be observed as a footprint of the laser used during the process. At high magnification, it can be seen the principal phase, austenite, appeared as columnar grains. On the other hand, there was segregation of the ferrite stabilizing elements, such as chromium or molybdenum, which can propitiate the nucleation of ferrite, as a secondary phase, in the grain borders [41,42]. These grains are smaller in the limit of the melt pools, because of the faster cooling in that zone during the solidification. The presence of delta ferrite was not observed in DRX, indicating that it would only appear in a very low proportion or that it does not exist in our samples.

In Figs. 4b and 5b, it can be seen the microstructure of the SS/SLM/400 sample and in Figs. 4c and 5c, it can be observed the microstructure of the SS/SLM/650 one. In both cases, the microstructure is like the as-SS/SLM: There is still a presence of columnar grains of austenite. The only difference is the grain size, which has grown with the increment of temperature. In this way, the biggest grains are present in the SS/SLM/

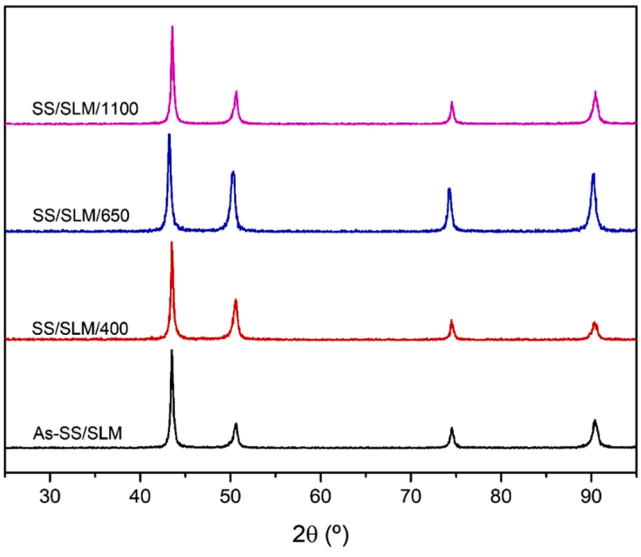

Fig. 2. XRD patterns of the 316 L SLM sample and the three heat-treated samples.

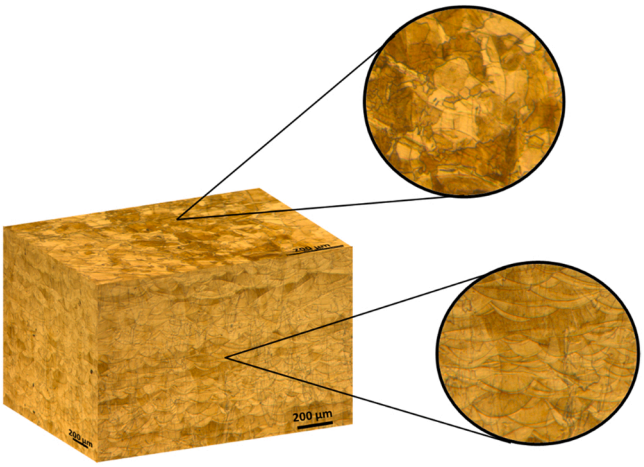

Fig. 3. Optical micrographs at 100 magnifications of as-SS/SLM sample.

650 specimen. Other studies have found that, in this case, there are other effects like the reduction of the residual stress with the increment of temperature [43].

Finally, in Figs. 4d and 5d it can be seen the microstructure of the SS/SLM/1100 sample. In this case, the structure of columnar grains has changed to a microstructure formed by austenitic equiaxial grains [44], due to the recrystallization and growth of new grains [24]. Due to the high temperatures, the delta ferrite dissolves partially provoking microsegregation of elements like chromium, molybdenum, or manganese. The microsegregation can provoke the apparition of a new phase, sigma ferrite, at 800 °C [24], which could grow from the grain boundaries to the inner of the grains [45]. In contrast, these ferritic phases have not been found by SEM, so TEM was required to confirm the composition of the different phases.

Fig. 6 shows the general views of the different specimens observed by STEM-EDS. In the as-SS/SLM, SS/SLM/400, and SS/SLM/650 (Fig. 6a, b, and c, respectively), different nanoinclusions can be seen, as shown by other authors in previous studies [46,47]. These spherical nanoinclusions were mainly attributed to the accumulation of elements like oxygen, silicon, manganese [40], aluminum [48], and nitrogen [49]. Besides these inclusions, only austenite was detected, as is shown in the diffraction pattern in Fig. 7, which corresponds to an FCC structure. In this pattern, it can be seen a slight modification of the interplanar distance because the structure has more elements besides the iron. On the other hand, in the SS/SLM/1100, Fig. 6d, other precipitates with irregular and angular geometry were observed, besides the mentioned nanoinclusions.

The precipitates found in the SS/SLM/1100 were richer in chromium and manganese than the austenite matrix, similar to the nanoinclusions, as shown in Fig. 8(a), general microstructure observed by STEM; b) EDS spectra of the matrix and the inclusions; and c) EDS of the difference of both spectra). Several authors, like Laleh et al. [40] and Wang et al. [49], have claimed that this composition is attributed to the existence of manganese chromite spinel, $MnCr_2O_4$. Laleh et al. claimed that they also found MnS inclusions in their heat-treated specimens. However, in this study, these MnS inclusions have not been found, but their presence cannot be discarded. Other authors, like Wang et al. [50], and Saeidi et al. [51] found phases like ferrite, but this is not the case in this study. In any case, all the authors coincide that heat treatment at 1100 °C caused the apparition of phases that do not exist in the as-built samples. Also, in the TEM studied specimens, it was observed a reduction in the number of dislocations with the increment of temperature. These dislocations mainly originated from the rapid solidification induced material deformation, and their diminution was observed at temperatures above 650 °C, as other authors claimed [49], although we have also observed this reduction at lower temperatures, i.e., 400 °C.

3.2. Porosity, density, and hardness

A general study of the defects of the parts has been carried out. In the evaluated parts, defects like lack of fusion have not been found, but a small amount of porosity was observed. The values of porosity and grain size for the samples manufactured and heat-treated are shown in Fig. 9. The density of the samples after the heat treatments (blue squares) decreased with the temperature of the heat treatments provided, which is related to an increment of the porosity. And due to this, porosity more than doubled by treating the samples at 400 °C, tripled after the 650 °C treatment, and showed a four-some increase after the 1100 °C

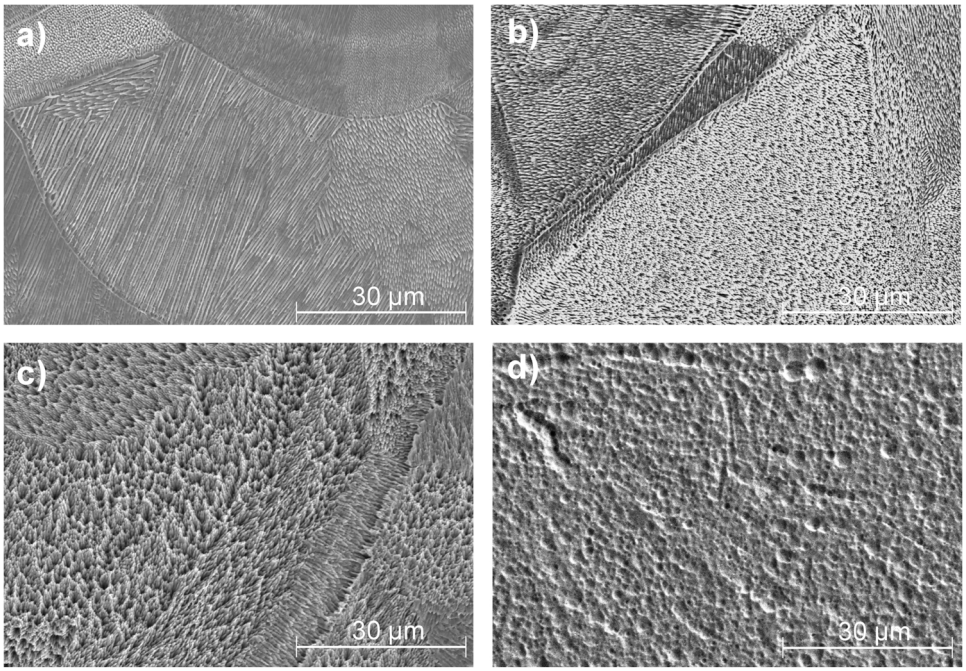

Fig. 4. SEM micrographs of a) as-SS/SLM, b) SS/SLM/400, c) SS/SLM/650 and d) SS/SLM/1100.

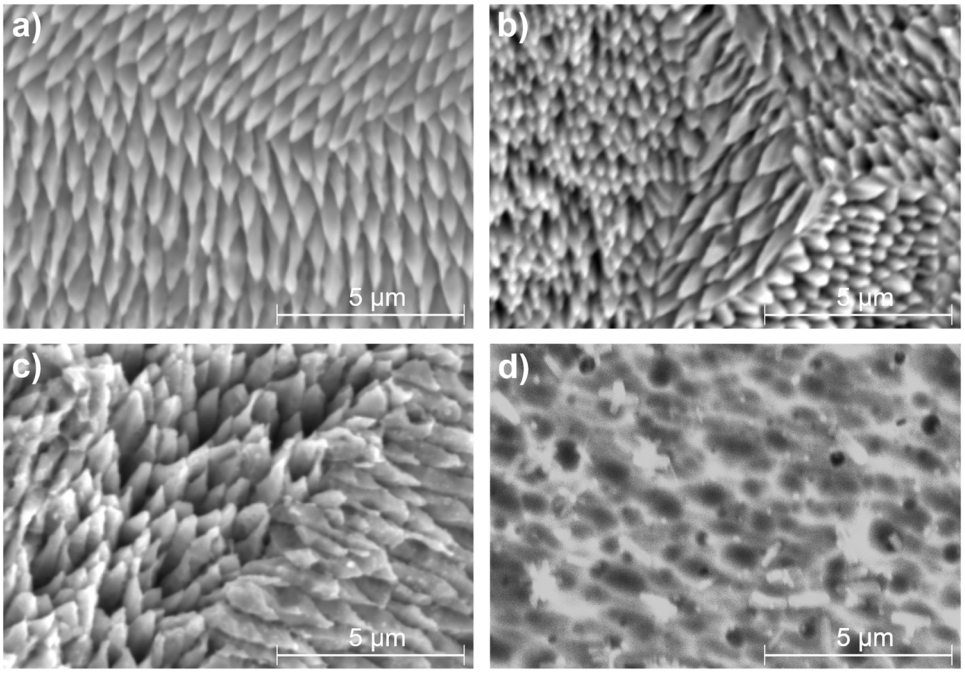

Fig. 5. SEM micrographs at higher magnifications of a) as-SS/SLM, b) SS/SLM/400, c) SS/SLM/650 and d) SS/SLM/1100.

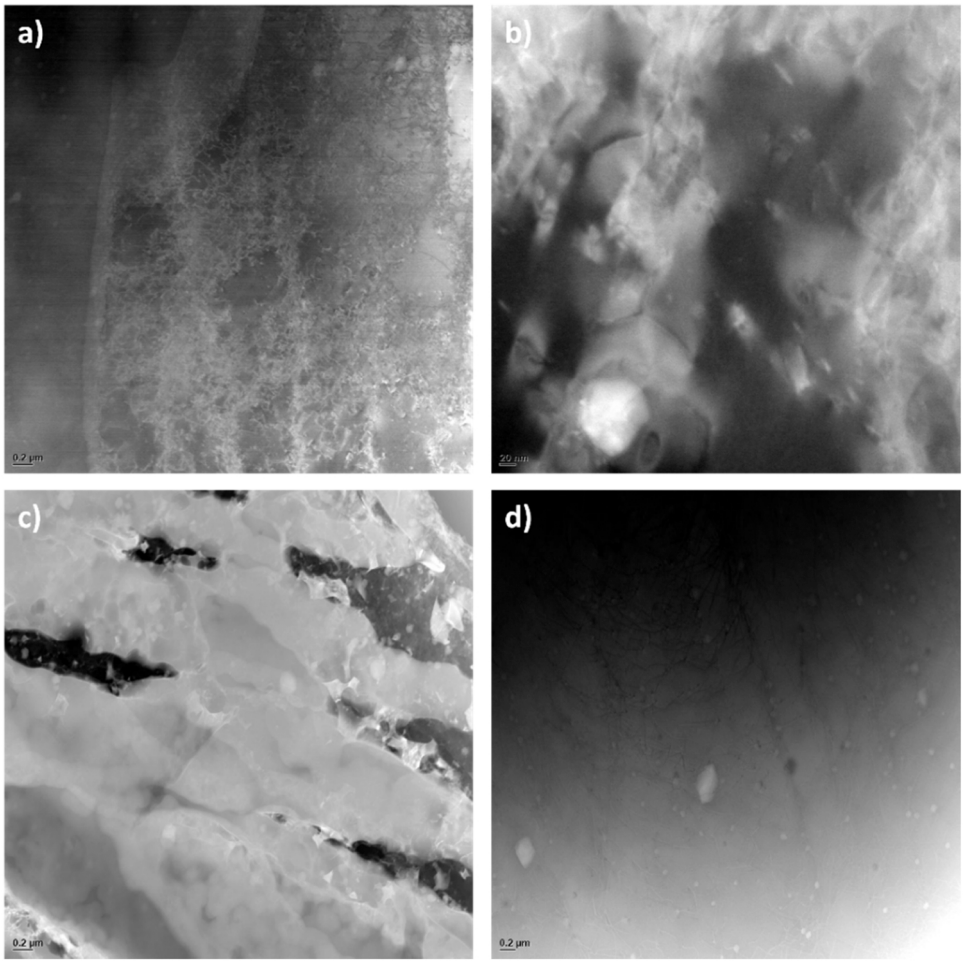

Fig. 6. STEM images of a) as-SS/SLM, b) SS/SLM/400, c) SS/SLM/650 and d) SS/SLM/1100.

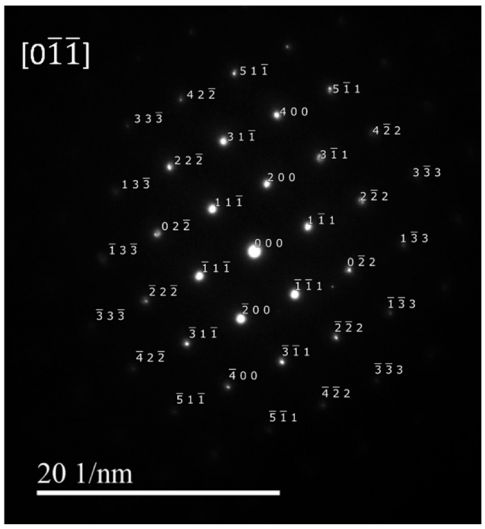

Fig. 7. Diffraction pattern of the matrix found in every studied specimen, in this case, in the SS/SLM/1100.

treatment. This phenomenon can be explained as the pores observed by optical microscopy were formed by the presence of trapped gas in the microstructure during manufacturing, which, in some cases, comes from the vaporization of elements of the alloy. In other manufacturing processes, trapped gas comes from the incorporation of gases from the atmosphere into the microstructure. In this case, the defects observed were spherical, and with the heat treatments, they grew, indicating that there is trapped gas in the pores that expanded during heating. However, porosity in these samples was residual (less than 0.5% in every specimen as observed by optical microscopy), and the increase, although relatively important, has a negligible total value in many properties such as the mechanical ones. However, sometimes, small pores give rise to the initiation of corrosion mechanisms, and it is important to evaluate their influence. Fig. 10 shows the general surface state of each type of specimen before the corrosion tests, showing the increment of the porosity in the SS/SLM/650, c; and SS/SLM/1100, d; specimens with regard to the as-SS/SLM, a; and SS/SLM/400, b; samples.

On the other hand, the grain size of the material grew with the heat treatments applied, as it is shown by the red diamonds in Fig. 9, which show a reduction in the grain size number, *G*. After the 400 °C heat treatment, the grain size showed a split behavior that resulted in very

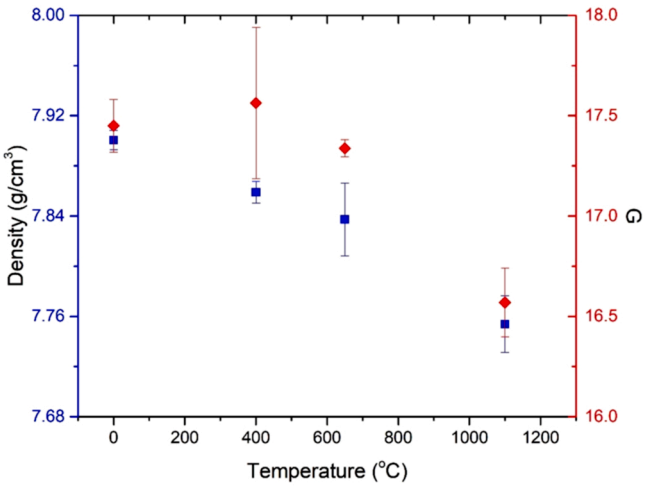

Fig. 9. Results of the density and the grain size number, *G*, depending on the temperature of the heat-treatment applied.

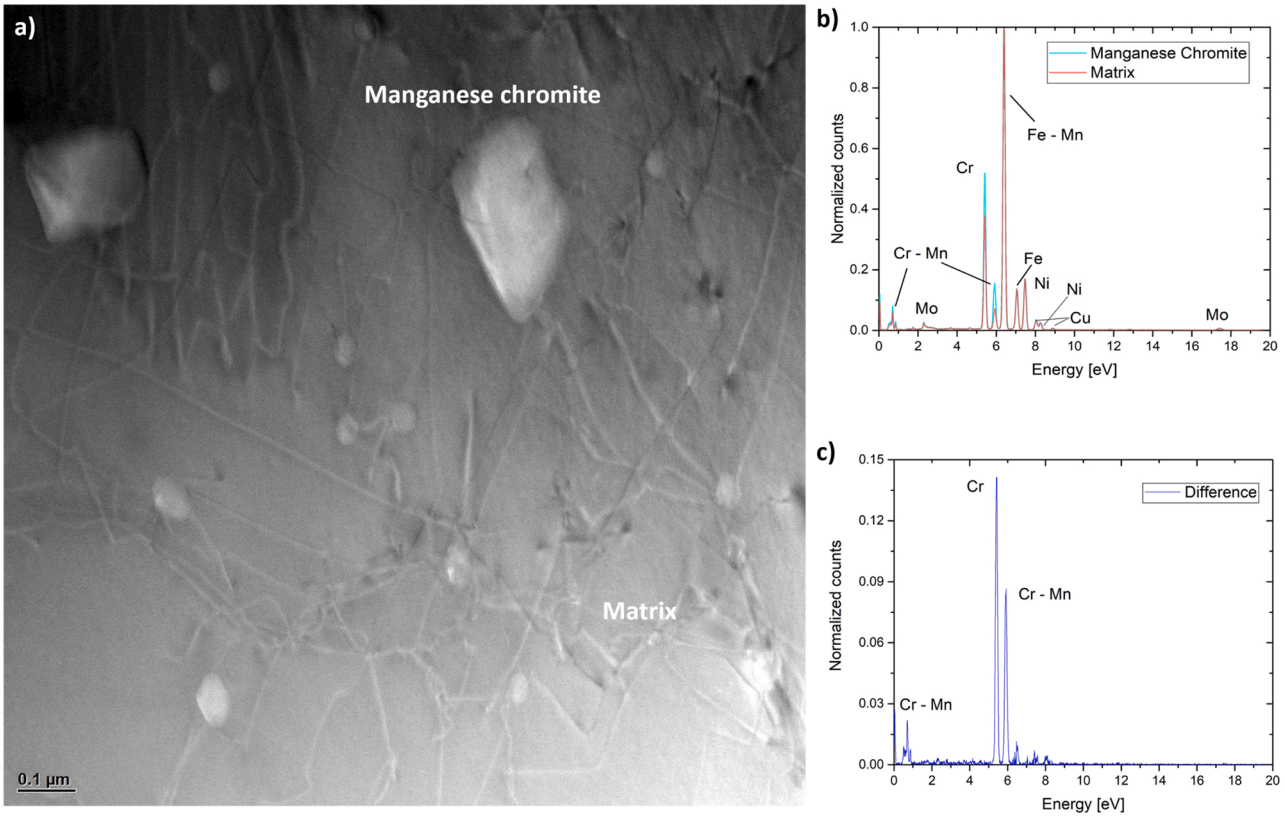

Fig. 8. STEM-EDS analysis of the phases found in the SS/SLM/1100 specimen: a) STEM image of the general microstructure; b) EDS spectra of the matrix and the manganese chromite; and c) difference of both EDS spectra.

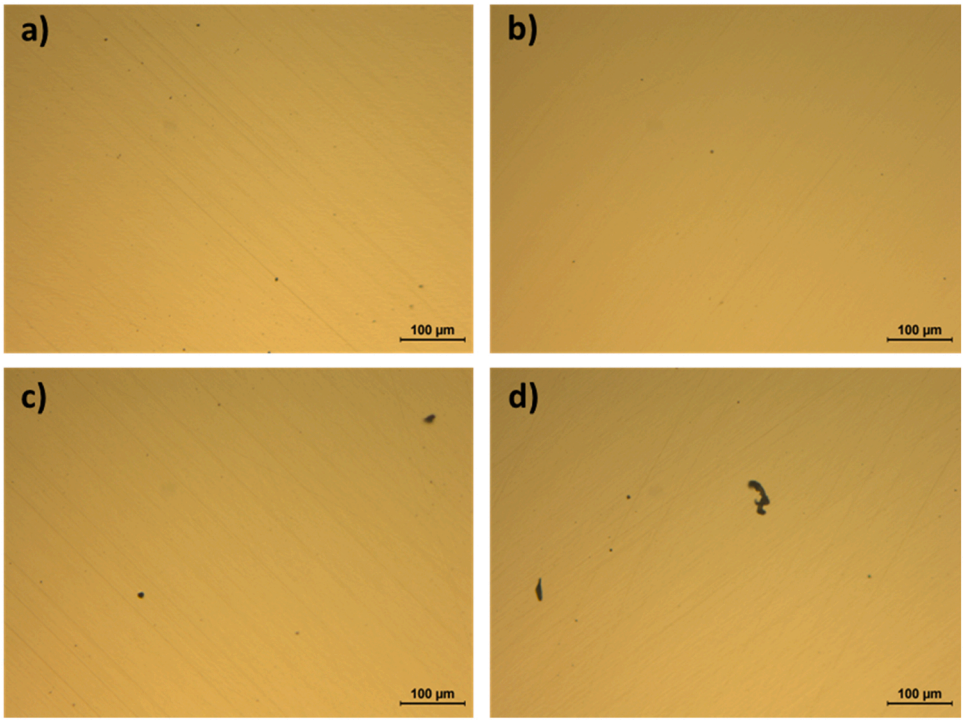

Fig. 10. Surface state of the samples before the corrosion tests: a) as-SS/SLM, b) SS/SLM/400, c) SS/SLM/650 and d) SS/SLM/1100.

large uncertainty in the measurements. This indicates that some grains seem to reduce while others grow. This observation can be explained from the perspective of the initiation of a recrystallization process that is characteristic of systems that show a high number of defects. In these types of systems, new crystals of small size appear in zones that show many defects, in the first instances, these grains are small, but with time they grow to sizes larger than the initial ones. Therefore, in our system, there seems that the grain structure was growing through a recrystallization process. After the heat treatment at 650 °C, the grain size shows a homogenization, characterized by a small standard deviation, and an increase in size. Finally, after the heat treatment at 1100 °C, the grain size was larger as the grain number, *G*, reduced.

This behavior has been also observed in other studies [46], and it is attributed to the recrystallization that the specimen suffers under this temperature [48]. Some authors have claimed that there is an interaction between the porosity and the grain size of the stainless steel once it is treated [47]. In this case, the coarsening of the microstructure during the heat treatment provoke small rounded pores (Fig. 5d), as shown in other studies [52].

The results of the hardness testing are plotted in Fig. 11 along with the grain size number. There was a clear similitude of both magnitudes as both show the same tendencies. An increment of the temperature of the heat treatment caused the coarsening of the microstructure, which provokes a reduction of the hardness that can be explained through the Hall–Petch effect, which indicates that the reduction of the grain boundaries, which presents a resistance to the transmission of slip from one grain to the next.

Large dispersion of the hardness values was observed. A similar dispersion was found in other studies [53] and is caused by the different orientations of the grains and the various phases present in the material.

3.3. Electrochemical analysis

3.3.1. Potentiodynamic polarization measurements

Polarization measurements of the as-SS/SLM and the heat-treated samples were carried out in 3.5 wt% NaCl. Fig. 12a shows the evolution of the polarization resistance values (*Rp*) of the different systems

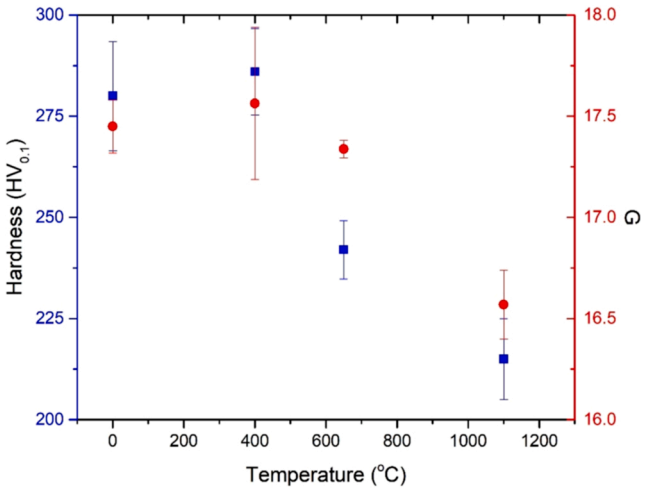

Fig. 11. Hardness ($HV_{0.1}$) and grain size number, *G*, for the temperature treatments used.

with the immersion time.

The *Rp* value of the untreated sample and the SS/SLM/400 one increased with immersion time, reaching an *Rp* value of about $6{\cdot}10^5$ Ω cm^2. The as-SS/SLM sample showed slower growth, increasing with the square root of time. The SS/SLM/400 showed a fast increase and reached its maximum value after only 24 h of immersion.

For the SS/SLM/650 and the SS/SLM/1100 samples, the *Rp* values decreased with the increase of the immersion time. This difference in the *Rp* values evolution indicates that different corrosion mechanisms were taking place in the different tested samples and that a change in the composition of the sample has happened.

Also, the initial *Rp* values strongly differed between samples. The lowest *Rp* value was obtained for the SS/SLM/400 sample after 1 h of immersion in NaCl, showing a value of about $3.35{\cdot}10^4$ Ω cm^2. At this time, the results obtained for the as-SS/SLM, SS/SLM/650, and SS/SLM/

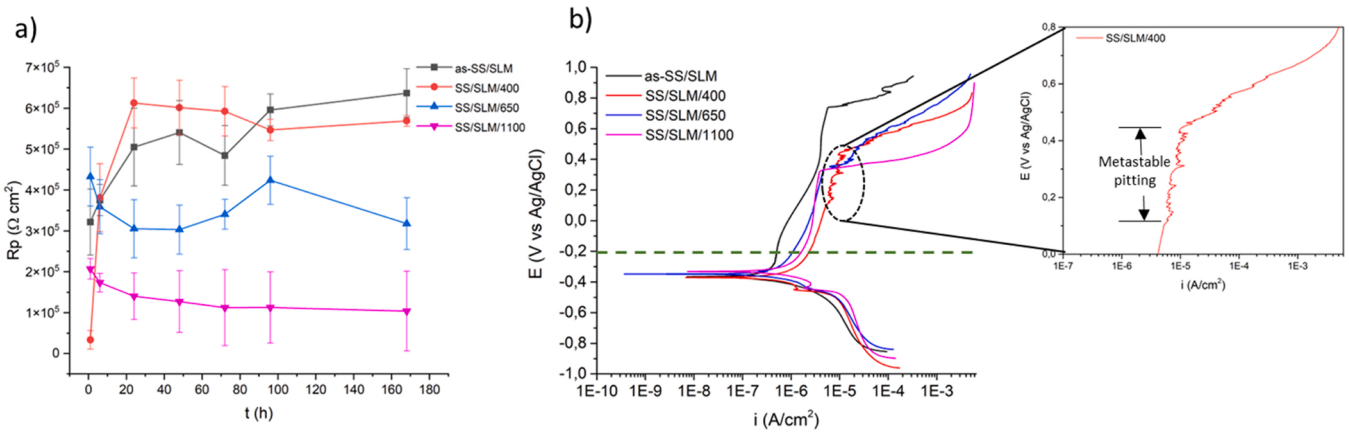

Fig. 12. Electrochemical results of the SLM specimens tested in 3.5 wt% NaCl solution a) polarization resistance (*Rp*) vs immersion time b) Tafel curves after 1 h immersion.

1100 samples were $3.21{\cdot}10^5$ Ω cm^2, $4.32{\cdot}10^5$ Ω cm^2, and $2.07{\cdot}10^5$ Ω cm^2, respectively, i.e., were nearly one order of magnitude higher. From this time on, the lowest *Rp* values corresponded to the SS/SLM/1100 sample at every immersion time.

Anodic-cathodic polarization tests were made in 3.5 wt% NaCl aqueous solution after 1 h of stabilization time. The obtained curves of the untreated and the heat-treated stainless-steel samples are shown in Fig. 12b. The horizontal dashed line in Fig. 8b represents the corrosion potential of a bulk 316 L stainless steel plate and is plotted for comparison. Table 2 shows the Open Circuit Potential (OCP), the corrosion potential (E_{corr}), and the corrosion current densities (i_{corr}) obtained using the intersection method in the Tafel curves. The analysis of the corrosion potential allowed obtaining the thermodynamic characteristics of the reaction systems.

A slightly difference in the E_{corr} values have been observed for the different tested samples, and the potential reduced with the treatment temperature. The difference observed may be related with the differences in the oxygen limit current density, as the tests were carried out in aerated solution in stagnant conditions. All the values differed from the corrosion potential of the 316 L bulk stainless-steel material (–0.2 V) used as a reference, and the difference slightly decreased with the high-temperature heat treatments.

The corrosion density is indicative of the corrosion kinetics of the system. The lowest i_{corr} was obtained for the as-SS/SLM sample (0.213 μA/cm^2). The heat-treated samples showed higher corrosion densities, 1.33 μA/cm^2, 0.967 μA/cm^2 and 0.539 μA/cm^2 for SS/SLM/400, SS/SLM/650 and SS/SLM/1100 samples, respectively. Therefore, the greater the temperature of the heat treatment, the lower the corrosion density of the samples; except for the as-built SLM samples. These results evidence that the heat treatments do not improve the corrosion behavior of the SLM stainless steel as measured from the electrochemical tests.

The anodic regions of the different curves (Fig. 12b) were characterized by a constant current density zone followed by an abrupt current density increase, which indicates the passive and the passive film breakdown behaviors. The SS/SLM/400 sample showed anodic current fluctuations (inset in Fig. 12b) which are related to metastable pitting. Although these fluctuations were also observed in the other samples, for SS/SLM/400 sample the metastable pitting was more prominent. For the as-SS/SLM sample, the changes in the current density observed at potentials near 0.7 V were related to the oxygen evolution. Also, the dispersion observed within similar samples could be caused by differences in porosity and precipitates formed in each sample, confirming their role played in localized corrosion.

Table 2
Open Circuit Potential (OCP) and corrosion densities (i_{corr}) of the specimens tested in 3.5 wt% NaCl from the anodic-cathodic corrosion test after 1 h immersion.

Sample	OCP (V)	Ecorr (V)	icorr (μA/cm2)
as-SS/SLM	-0.13 ± 0.02	-0.37 ± 0.05	0.21 ± 0.05
SS/SLM/400	-0.17 ± 0.01	-0.37 ± 0.03	1.33 ± 0.13
SS/SLM/650	-0.04 ± 0.02	-0.35 ± 0.03	0.67 ± 0.11
SS/SLM/1100	-0.10 ± 0.01	-0.33 ± 0.02	0.54 ± 0.05

Cyclic polarization tests were also carried out (Fig. 13). The curves show that the specimens treated at 400 °C and the as-built parts immersed in 3.5% NaCl for one hour did not suffer pitting corrosion during the test as the curve at its top shows a strong reduction in the current density when the potential slightly reduces. On the other hand, the curves of the samples treated at higher temperatures suggest the presence of pitting corrosion as the curve shows a small amount of hysteresis at the higher potential values. The surface morphologies of the different samples after the immersion test are shown in Fig. 14. No pits were observed on the surfaces of the as-ss/SLM and SS/SLM/400 samples as shown in Fig. 14 a and b, respectively. Otherwise, the analysis of the surfaces of the SS/SLM/650 and SS/SLM/1100 samples (Fig. 14 c and d) revealed the presence of pits with a diameter that in some cases surpasses 100 μm.

In the case of the SS/SLM/1100 specimen, the irregular geometry of the $MnCr_2O_4$ and the presence of other phases like MnS caused by the high temperature treatment [37,54], are responsible for the formation of a Cr-depletion zone that weakened them so that they can act as pit initiation site [36,38–40]. Specifically, Laleh et al. found that inclusions formed by Mn and S act as pits initiators since they dissolve from the interface to the matrix to the inner of them [40]. Also, Wang et al. found that these inclusions act as nucleation sites for the pitting corrosion, reducing the corrosion resistance of the 316 stainless steel [49]. On the other hand, Chao et al. made a bibliographic study on the role of inclusions as pits initiators and, although they claimed that these inclusions were the cause of pitting corrosion, they were not sure on the mechanisms involved [55]. This behavior of the oxide is not found in the spherical nanoinclusions, so the behavior of the spherical inclusions is not detrimental, as the same authors confirm. On the other hand, the SLM technique, due to the fast cooling of the melted layers, avoids the Cr-depletion zones that 316 L stainless steel has when it is fabricated by other manufacturing methods, so the apparition of these pitting initiating zones is avoided. Finally, zones with pores have been found to be pitting-sensitive sites since they provide diffusion mechanisms that worsen the corrosion resistance [36]. This fact can cause inconsistency in the corrosion performance, as can be seen in the deviation of the cyclic polarization values [54].

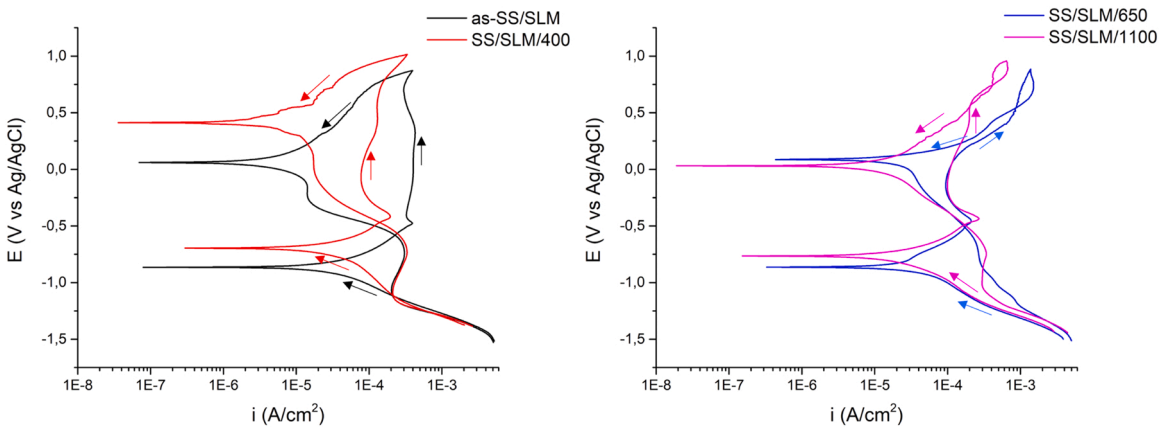

Fig. 13. Cyclic potentiodynamic polarization curves of the as-SS/SLM and the heat-treated LPBF samples.

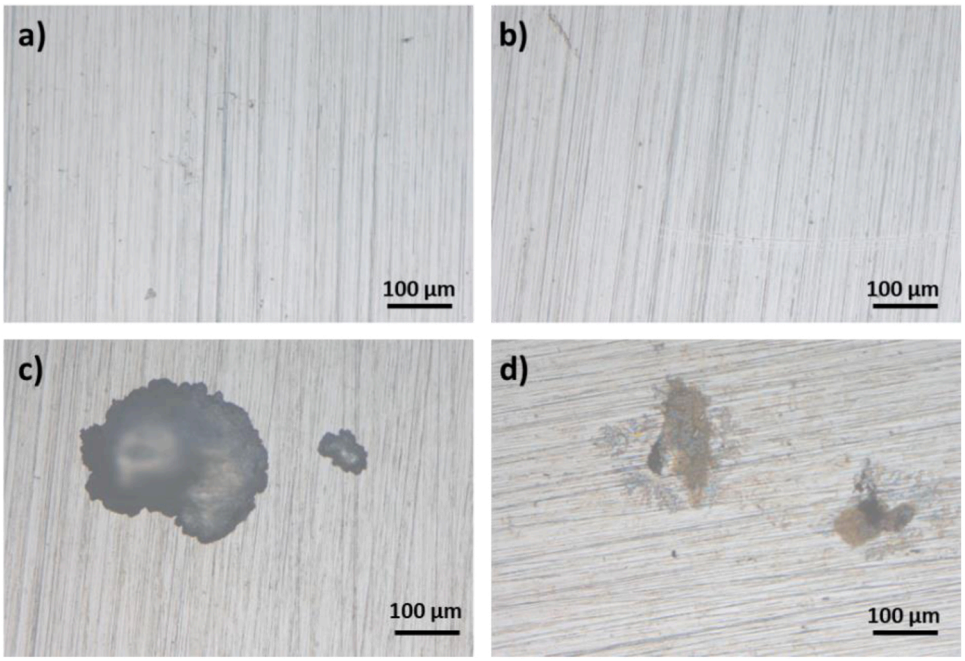

Fig. 14. Surface morphology of a) as-SS/SLM, b) SS/SLM/400, c) SS/SLM/650 and d) SS/SLM/1100 samples after the cyclic potentiodynamic polarization test.

3.3.2. Electrochemical impedance spectroscopy (EIS)

The Nyquist and Bode plots for the EIS of the as-SS/SLM sample and the heat-treated alloys in 3.5 wt% NaCl solution at the different immersion times up to 168 h are shown in Fig. 15. The curves shown are characteristic results for the test made by triplicate in the samples. The results obtained can be used to estimate the stability of the oxide film on the additive manufactured stainless steel sample when heat treatments are carried out. The Nyquist plots of all tested samples showed partial capacitive semicircles regardless of the sample and the immersion time used. This indicates that corrosion is controlled through charge transference and not mass transference. Therefore, there were no diffusion mechanisms present in the corrosion diagrams. In this context, the greater the diameter of the apparent semicircle, the greater the resistance to electrochemical dissolution and the greater the stability of the passive film. Also, the Bode plots provide the modulus of the electrochemical impedance and allow the evaluation of the behavior of the samples.

In the Bode-phase plots vs frequency, the phase angles were always smaller than 90°. The contribution of the different frequencies to the corrosion impedance was similar in all the systems at every immersion time. Only differences in the phase diagram were observed for the as-built and heat-treated at 400 °C for the shorter immersion time. These samples showed lower phase values at high frequencies, which indicates that the answer of the system to the potential perturbation is dominated by the resistance of the solution (*Re*). On the other hand, when the frequencies were lower, the phase was higher, which indicates that the process was dominated by the resistance of the surface of the metal, i.e., R_1; the Constant Phase Element (CPE) Q_1; and R_2 and Q_2 in the cases in which they existed.

In the Bode diagrams of |Z| vs frequency, the impedance value obtained at the lowest frequency (10^{-2} Hz) indicates the barrier properties of the oxide layer. It can be observed that the total impedance of the matrix/film/solution system for the SS/SLM/400 sample was larger than for the other tested samples at all immersion times, followed by the as-SS/SLM sample. The as-built and heat-treated at 400 °C showed a strong evolution of the corrosion impedance from values slightly above 10^5 Ω cm^2 to $3{\cdot}10^5$ Ω cm^2 and $5{\cdot}10^5$ Ω cm^2, respectively. The samples treated at higher temperatures showed very similar curves and values from the first immersion hour to 168 h. In both cases, the values were lower than those of the other samples, with maximum values of $0.5{\cdot}10^5$

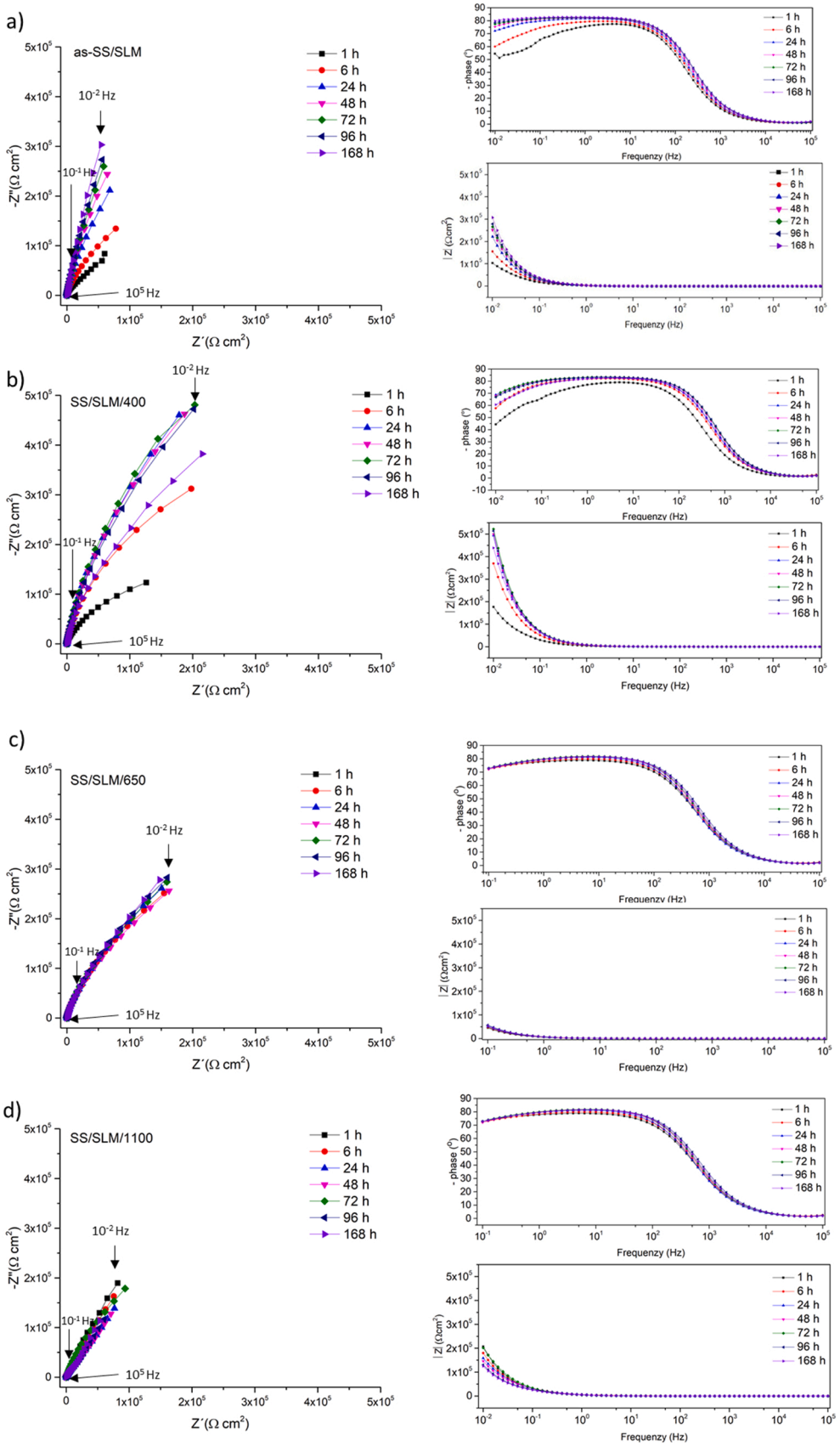

Fig. 15. Nyquist and Bode plots of the EIS spectra for the corrosion at different immersion times of the samples: a) as-SS/SLM, b) SS/SLM/400, c) SS/SLM/650, and d) SS/SLM/1100.

Ω cm^2 for the sample treated at 650 °C, and 2·10^5 Ω cm^2 for the one treated at 1100 °C. For each sample, this value increased with the increase of the immersion time, except for the SS/SLM/1100 sample, where the maximum value was reached after 72 h of immersion. These results are in good agreement with the anodic polarization experiments, where higher polarization resistance and a much larger passive region were observed for as-SS/SLM and SS/SLM/400 samples compared to the other samples.

Despite the differences in values observed, the most relevant data is the diameter of the capacitive circle, which seems similar in both cases, and requires fitting. To do so, two equivalent electric circuits (EECs) related to the microstructure of the passive films on stainless steel were proposed (Fig. 16). These circuits change depending on the heat treatment. On the one hand, the treatment at 400 °C kept the regularity and the homogeneity of the passive layer that the parts have without heat treatment. In this case, the circuit which fits the EIS curves is the one shown in Fig. 16 a with one time constant: *Re* for the resistance of the solution, and R_1 and the CPE Q_1 for the impedance of the passive layer. On the other hand, as mentioned before, treatments at the highest temperature increased the porosity and caused the apparition of chromium-depletion zones, which weaken the passive layer. All of this makes a weaker surface of the 316 L stainless steel, resulting in the circuit of Fig. 16 b, which has two time constants and is used for porous films: in addition to the elements mentioned before, this circuit has two other elements, R_2 and the CPE Q_2, associated with the irregularities of the surface passive layer [56]. A constant phase element (CPE) in an equivalent circuit that imitates the behavior of an imperfect capacitor, with an impedance defined by:

$$Z_{CPE} = [Q(j\omega)^n]^{-1} \tag{3}$$

where Q is the capacitance, ω is the angular frequency and n is a factor that estimates the deviation of the system from ideal capacitive behavior [57]. When n = 1, CPE describes an ideal capacitor and Q is the capacitance C. When n = 0.5, the CPE is a Warburg impedance related to the ionic flux across the film, which is corresponding to the porous electrode [57].

A good fit was achieved between the experimental results and the equivalent circuits proposed. The values of the impedance parameters R_e, R_1, Q_1, n_1, R_2, Q_2, and n_2 from the fitting of the different equivalent circuits for the different samples are shown in Table 3. It can be observed that the fitting using two time constants in the equivalent circuit was possible only for the results obtained at 1 h of immersion for all tested samples and the SS/SLM/650 and SS/SLM/1100 samples, regardless of the immersion time. In this model, during the process of coverage, the film previously formed can suffer important changes in its properties, such as thickness, crystallinity, resistivity, or capacity. So this model proposes the growth and destruction of the passive film [58]. The fitting suggests that the passive film formed in SS/SLM/650 and SS/SLM/1100 samples had defects and this caused its low corrosion resistance. The $_{Re}$ value, which represents the electrolyte bulk resistance, was approximately 20 Ω·cm^2 in all tested samples. This value corresponds to the intersection of the capacitive semicircle with the real axis at high frequencies in the Nyquist plots. R_1 and Q_1 evaluate the behavior of the passive film formed. Q_1 represents the capacity behavior of the passive

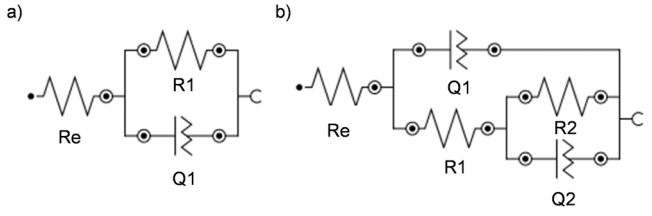

Fig. 16. Proposed equivalent circuit for the AM heat-treated specimens: a) for as-SS/SLM and SS/SLM/400 and b) for SS/SLM/650 and SS/SLM/1100.

film and R_1 is related to the resistance due to the ionic paths through the oxide film. In the second process, Q_2 represents the capacitive behavior at the double layer in the interfaces and R_2 the charge-transfer resistance. The R_1 values were higher for as-SS/SLM and SS/SLM/400 samples than for SS/SLM/650 and SS/SLM/1100 samples which demonstrate the higher protection obtained for these samples. The Q_1 values obtained, which indicate the compactness of the film (the smaller the value, the more compact the layer), suggest that similar compactness was obtained.

These circuits are also employed to quantify the charge transfer resistance and the charge distribution within the electrical double layer. Graphs of these values are represented in Fig. 17. In Fig. 17 a, it can be seen the evolution of the element R_1, associated with the resistance of the passive layer which, as mentioned before, is weaker when the parts have had heat treatments at high temperatures, while the treatments at low temperature maintain a similar resistance of the passive layer as the parts without heat treatment. However, the resistance R_1 of the SS/SLM/400, besides being smaller than the of as-SS/SLM, reduced with time for the last hours of the test, something that does not happen in the case of the parts without heat treatment, but which showed lower resistance values.

In Fig. 17 b, it can be seen the evolution of the CPE Q_1. When this element declines, the resistance of the passive layer increases. This happened in all the samples except in the case of the SS/SLM/1100, which had a nearly constant Q_1 value that slightly increases with time. This result, according to the facts mentioned before, shows that the passive layer of the parts treated at high temperatures was weaker. This fact was related with several factors. The apparition of chromium -depletion zones provides local sites for corrosion pits. This fact weakens the passive layer. Moreover, the resistance of the passive layer, the R1 factor, obtained for as-SS/SLM sample was greater than that obtained for SS/SLM/1100 at all immersion times. Furthermore, the impedance diagram obtained for the SS/SLM/1100 sample was more complex than the one obtained for th as-SS/SLM sample, showing that more than one exponential is involved in the description of the mechanism of the system. So, for the SS/SLM/1100 sample we use the equivalent circuit of a porous layer to obtain a good fit of the impedance diagram. This fact affect the Q1 value obtained.

The thickness of the passive film can be obtained by the capacitance value, as authors like Brug et al. [59] and Hirschorn et al. [60] claim. The effective capacitance (C_{eff}) of the surface layer associated with the CPE can be expressed as:

$$C_{eff} = Q^{1/n} R_1^{(1-n)/n} \tag{4}$$

The capacitance can be related to film thickness (d_{eff}) according to:

$$C_{eff} = \frac{\varepsilon \quad \varepsilon_0}{d_{eff}} \tag{5}$$

where ε is the dielectric constant of the film, ε_0 is the permittivity of the free space (8.85·10^{-14} F/cm) [60]. The dielectric constant of chromium oxide and iron oxide is 12 [61]. The results obtained for the effective capacitance and the thickness of oxide films formed on the different heat-treated samples at different immersion times are shown in Table 4. To facilitate an understanding of the results, the δ values are shown in Fig. 18. The thickness of the oxide layer increased with the increase of the immersion time for all samples suggesting more formation of Fe-oxide and hydroxides on the external surface of the passive layer. From 24 h, the values stabilize, and higher thicknesses were obtained for SS/SLM/650 and SS/SLM/1100 samples. Although the thickness of the oxide films of these samples is higher than that obtained for as-SS/SLM and SS/SLM/400 samples, the protection that they offer is lower and this is related with the formation of porous hydroxides layer [62].

The evolution observed by EIS in the different systems corresponds well with that observed in the Tafel measurements. The behavior of the as-SS/SLM samples is characteristic of a structure in which there is a

Table 3
Impedance parameters from the equivalent circuits fitting for the different samples.

Sample	Immersion time (h)	$_{Re}$ (Ω • cm^2)	$R_1 \times 10^6$ (Ω • cm^2)	$Q_1 \times 10^{-5}$ (Ω•cm^2•s^n)	n_1	$R_2 \times 10^6$ (Ω • cm^2)	$Q_2 \times 10^{-5}$ (Ω•cm^2•s^n)	n_2
As-SS/SLM	1	24.0	0.01	6.79	0.90	1.35	1.78	0.33
	6	22.7	2.18	3.96	0.89			
	24	23.5	2.90	3.66	0.90			
	48	23.1	4.40	3.48	0.89			
	72	22.4	3.48	3.39	0.90			
	96	22.8	4.06	3.23	0.90			
	168	24.6	4.82	3.18	0.91			
SS/SLM/400	1	20.5	0.10	4.46	0.91	0.15	2.97	0.92
	6	19.7	0.77	2.98	0.92			
	24	20.6	1.67	2.42	0.93			
	48	18.9	1.67	2.40	0.93			
	72	19.2	1.79	2.25	0.93			
	96	18.7	1.51	2.26	0.93			
	168	22.7	1.00	2.37	0.92			
SS/SLM/650	1	20.1	0.33	3.19	0.89			
	6	20.1	0.02	2.63	0.92	10.0	5.15	0.40
	24	20.5	0.0041	2.44	0.93	36.2	5.81	0.41
	48	19.1	0.028	2.37	0.93	100.0	0.59	0.40
	72	19.5	0.0082	2.25	0.94	100.0	0.61	0.44
	96	19.2	0.10	2.02	0.94	50.0	0.67	0.47
	168	19.0	0.0068	2.21	0.94	10.5	0.67	0.47
SS/SLM/1100	1	17.4	2630	2.55	0.90	1.64	1.95	0.68
	6	16.7	3100	2.66	0.91	1.28	1.94	0.68
	24	17.3	0.0028	2.77	0.91	1.04	1.71	0.70
	48	17.1	0.0029	2.74	0.92	1.06	1.65	0.71
	72	16.7	0.0031	2.79	0.92	0.98	1.67	0.71
	96	16.5	0.0031	2.81	0.92	1.03	1.68	0.71
	168	15.6	0.0033	2.82	0.92	1.08	1.62	0.72

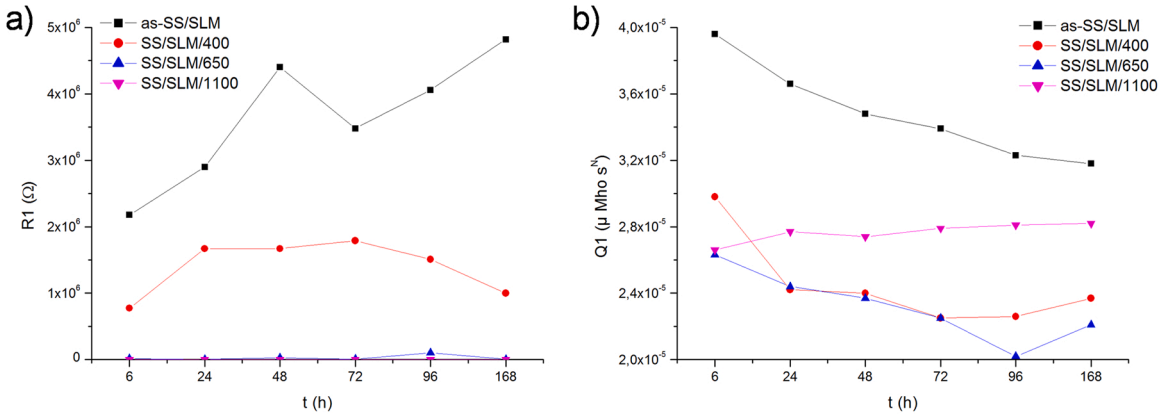

Fig. 17. Evolution of the values of a) *R1* and b) *Q1* for every sample.

Table 4
Effective capacitance and thickness of oxide films formed on the different heat-treated samples at the different immersion times.

Sample	As-SS/SLM						
Immersion time (h)	**1**	**6**	**24**	**48**	**72**	**96**	**168**
C_{eff} (μF/cm^2)	65.0	68.7	61.5	64.8	57.6	55.5	52.3
δ (nm)	1.6	1.6	1.7	1.6	1.8	1.9	2.0
Sample	**SS/SLM/400**						
C_{eff} (μF/cm^2)	51.7	39.1	32.0	31.7	29.7	29.5	31.2
δ (nm)	2.1	2.7	3.3	3.4	3.6	3.6	3.4
Sample	**SS/SLM/650**						
C_{eff} (μF/cm^2)	42.7	24.9	20.5	23.0	20.2	21.1	19.6
δ (nm)	2.5	4.3	5.2	4.6	5.3	5.0	5.4
Sample	**SS/SLM/1100**						
C_{eff} (μF/cm^2)	87.7	81.5	21.5	22.0	22.6	22.7	22.9
δ (nm)	1.2	1.3	4.9	4.8	4.7	4.7	4.6

homogeneous corrosion behavior, despite the characteristic microstructure of the SLM process. Apart from this, it does not seem to be zones that would cause the formation of a weak passive layer, which appears as a low corrosion intensity and high *R1* resistance values. The evolution with time of the different variables indicates that the passive layer grows with time without relevant defects. When heat treatments were applied the corrosion behavior was modified and both, Tafel and EIS, showed a reduction in the corrosion resistance. In the SS/SLM/400 case, the corrosion intensity grew in a similar amount as *R1* reduced, but the OCP remained constant and there no new mechanisms were revealed by EIS. This indicates that there were no new phases formed in the alloy and that the corrosion process was not significantly changed. The changes in the values can be explained as the result of the growth of the grain size observed, which also caused a reduction of the hardness and a possible increase in the chromium carbides size [46].

At higher temperatures of the heat treatment, i.e., 650 °C and 1100 °C, it was observed that the OCP changed and that EIS needed the addition of new elements in the equivalent circuit. This behavior is indicative of the presence of new phases and changes in the local

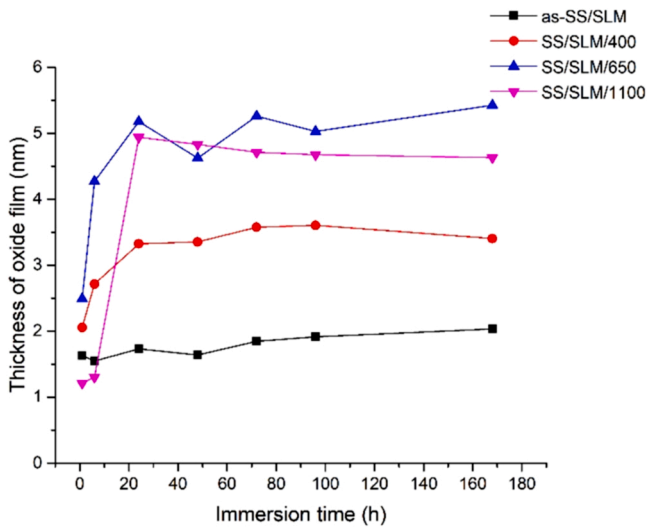

Fig. 18. Thickness of the oxide films of the different samples vs immersion time.

composition of the stainless steel. This was also suggested by the apparition of sensitivity to pitting corrosion in the cyclic corrosion tests. These results suggest that the segregation of elements causing the formation of new phases, such as MnS, and the formation of zones with depletion of chromium appeared in the samples due to the high temperatures used [39]. Therefore, in these conditions a passive layer is formed, while there is a passive layer breakdown in the vicinity of the Mn-chromite particles because of the reduction of Cr.

The influence of the heat treatments is very significant in the corrosion behavior of the 316 L stainless steel. The election of the heat treatment is important for the mechanical properties and also for the corrosion performance of the manufactured specimens. Therefore, it is essential to select a good heat treatment to reduce the defects and improve the mechanical properties without worsening the corrosion behavior of the parts by the formation of detrimental phases that could induce a new corrosion mechanism.

4. Conclusions

1. 316 L Stainless Steel parts fabricated by Laser Powder Bed Fusion were post-processed with different heat treatments to evaluate their influence on the microstructure, hardness, and corrosion behavior; progressing in the knowledge of the influence of these methods on the corrosion performance of the 316 L stainless steel.
2. Heat treatments caused the growth of the grain size, the increase in the porosity, and the decrease in the hardness. Also, the heat treatment at 1100 °C led to a microstructure change with the formation of inclusions of $MnCr_2O_4$.
3. The as-built part and the specimen treated at 400 °C showed an overall increase in the polarization resistance with the immersion time, especially in the first 24 h, while the specimens treated at a higher temperature started with a lower value and showed an overall decrease in this parameter. On the other hand, Tafel tests showed only small changes in the corrosion potential of the samples treated at higher temperatures, which also showed more corrosion intensity.
4. In the same way, samples treated at 650 °C and 1100 °C suffered pitting corrosion as shown in the cyclic polarization tests due to the apparition of other phases and intermetallic precipitates and the increment of the porosity. This phenomenon did not appear in the as-built parts and the specimens treated at 400 °C.
5. The samples treated at 650 °C and 1100 °C showed the presence of new phases and changes in the local composition of the stainless steel. The passive layers formed were thicker, but more porous and less protective. Also, local breakdown of the layer was observed in the sample treated at 1100 °C because of the presence of Mn-chromite inclusions.

CRediT authorship contribution statement

J. Bedmar: Methodology, Validation, Formal analysis, Investigation, Data curation, Writing – original draft, Visualization. **S. García-Rodríguez:** Methodology, Validation, Formal analysis, Investigation, Data curation, Writing – original draft, Visualization. **M. Roldán**: Methodology, Investigation. **B. Torres:** Conceptualization, Formal analysis, Investigation, Resources, Writing – review & editing, Visualization, Supervision, Project administration, Funding acquisition. **J. Rams:** Conceptualization, Formal analysis, Investigation, Resources, Writing – review & editing, Visualization, Supervision, Project administration, Funding acquisition.

Declaration of Competing Interest

The authors declare the following financial interests/personal relationships which may be considered as potential competing interests: J. Rams reports financial support was provided by Government of Spain Ministry of Finance and Public Administration. J. Rams reports financial support was provided by Comunidad de Madrid Consejeria de Economia y Hacienda.

Data availability

The raw/processed data required to reproduce these findings cannot be shared at this time due to technical or time limitations.

Acknowledgments

This work was supported by the Ministerio de Economía y Competitividad of Spain (Project RTI2018–096391-B-C31, PID2021–123891OB-I00, PID2021–124341OB-C21) and Comunidad de Madrid (Project S2018/NMT-4411). We acknowledge the National Fusion Laboratory of CIEMAT for the sample preparation. We also acknowledge the Electronic Microscopy National Center of the Complutense University of Madrid for the use of their JEOL 300 F microscope.

References

[1] M. Talib Mohammed, Mechanical properties of SLM-titanium materials for biomedical applications: a review, Mater. Today Proc. 5 (2018) 17906–17913, https://doi.org/10.1016/j.matpr.2018.06.119.
[2] N. Rahulan, S.S. Sharma, N. Rakesh, R. Sambhu, A short review on mechanical properties of SLM titanium alloys based on recent research works, Mater. Today Proc. (2021), https://doi.org/10.1016/j.matpr.2021.10.184.
[3] M. Seabra, J. Azevedo, A. Araújo, L. Reis, E. Pinto, N. Alves, R. Santos, J. Pedro Mortágua, Selective laser melting (SLM) and topology optimization for lighter aerospace componentes, Procedia Struct. Integr. 1 (2016) 289–296, https://doi.org/10.1016/j.prostr.2016.02.039.
[4] F. Bartolomeu, J. Fonseca, N. Peixinho, N. Alves, M. Gasik, F.S. Silva, G. Miranda, Predicting the output dimensions, porosity and elastic modulus of additive manufactured biomaterial structures targeting orthopedic implants, J. Mech. Behav. Biomed. Mater. 99 (2019) 104–117, https://doi.org/10.1016/j.jmbbm.2019.07.023.
[5] S. Chen, J. Wang, Z. Yuan, Z. Wang, D. Du, Microstructure and arc erosion behaviors of Ag-CuO contact material prepared by selective laser melting, J. Alloy. Compd. 860 (2021), 158494, https://doi.org/10.1016/j.jallcom.2020.158494.
[6] C. Galy, E. Le Guen, E. Lacoste, C. Arvieu, Main defects observed in aluminum alloy parts produced by SLM: From causes to consequences, Addit. Manuf. 22 (2018) 165–175, https://doi.org/10.1016/j.addma.2018.05.005.
[7] A. Tridello, J. Fiocchi, C.A. Biffi, G. Chiandussi, M. Rossetto, A. Tuissi, D.S. Paolino, Effect of microstructure, residual stresses and building orientation on the fatigue response up to 109 cycles of an SLM AlSi10Mg alloy, Int. J. Fatigue 137 (2020), 105659, https://doi.org/10.1016/j.ijfatigue.2020.105659.
[8] L. Pezzato, M. Dabalà, S. Gross, K. Brunelli, Effect of microstructure and porosity of AlSi10Mg alloy produced by selective laser melting on the corrosion properties of

plasma electrolytic oxidation coatings, Surf. Coat. Technol. 404 (2020), 126477, https://doi.org/10.1016/j.surfcoat.2020.126477.
[9] P. Promoppatum, R. Srinivasan, S.S. Quek, S. Msolli, S. Shukla, N.S. Johan, S. van der Veen, M.H. Jhon, Quantification and prediction of lack-of-fusion porosity in the high porosity regime during laser powder bed fusion of Ti-6Al-4V, J. Mater. Process. Technol. 300 (2022), 117426, https://doi.org/10.1016/j.jmatprotec.2021.117426.
[10] B.J.M. Freitas, V.A. de Oliveira, P. Gargarella, G.Y. Koga, C. Bolfarini, Microstructural characterization and wear resistance of boride-reinforced steel coatings produced by Selective Laser Melting (SLM), Surf. Coat. Technol. 426 (2021), 127779, https://doi.org/10.1016/j.surfcoat.2021.127779.
[11] A. Charmi, R. Falkenberg, L. Ávila, G. Mohr, K. Sommer, A. Ulbricht, M. Sprengel, R. Saliwan Neumann, B. Skrotzki, A. Evans, Mechanical anisotropy of additively manufactured stainless steel 316L: an experimental and numerical study, Mater. Sci. Eng. A. 799 (2021), 140154, https://doi.org/10.1016/j.msea.2020.140154.
[12] P. Mercelis, J. Kruth, Residual stresses in selective laser sintering and selective laser melting, Rapid Prototyp. J. 12 (2006) 254–265, https://doi.org/10.1108/13552540610707013.
[13] Ł. Szczepański, M. Bambach, F. Jensch, A. Ambroziak, T. Kurzynowski, Structural investigations of Fe-Zr-Si-Cu metallic glass with low glass-forming ability produced in laser powder bed fusion technology, Mater. Des. 210 (2021), 110112, https://doi.org/10.1016/j.matdes.2021.110112.
[14] Y. Wang, L. Zhang, X. Li, Z. Yan, On hot isostatic pressing sintering of fused filament fabricated 316L stainless steel – Evaluation of microstructure, porosity, and tensile properties, Mater. Lett. 296 (2021), 129854, https://doi.org/10.1016/j.matlet.2021.129854.
[15] M.K. Gupta, A.K. Singla, H. Ji, Q. Song, Z. Liu, W. Cai, M. Mia, N. Khanna, G. M. Krolczyk, Impact of layer rotation on micro-structure, grain size, surface integrity and mechanical behaviour of SLM Al-Si-10Mg alloy, J. Mater. Res. Technol. 9 (2020) 9506–9522, https://doi.org/10.1016/j.jmrt.2020.06.090.
[16] H.M. Hamza, K.M. Deen, W. Haider, Microstructural examination and corrosion behavior of selective laser melted and conventionally manufactured Ti6Al4V for dental applications, Mater. Sci. Eng. C. 113 (2020), 110980, https://doi.org/10.1016/j.msec.2020.110980.
[17] S. Beretta, M. Gargourimotlagh, S. Foletti, A. du Plessis, M. Riccio, Fatigue strength assessment of "as built" AlSi10Mg manufactured by SLM with different build orientations, Int. J. Fatigue 139 (2020), 105737, https://doi.org/10.1016/j.ijfatigue.2020.105737.
[18] K.S. Al-Rubaie, S. Melotti, A. Rabelo, J.M. Paiva, M.A. Elbestawi, S.C. Veldhuis, Machinability of SLM-produced Ti6Al4V titanium alloy parts, J. Manuf. Process. 57 (2020) 768–786, https://doi.org/10.1016/j.jmapro.2020.07.035.
[19] B. Zhang, M. Xiu, Y.T. Tan, J. Wei, P. Wang, Pitting corrosion of SLM Inconel 718 sample under surface and heat treatments, Appl. Surf. Sci. 490 (2019) 556–567, https://doi.org/10.1016/j.apsusc.2019.06.043.
[20] G. Ivetic, I. Meneghin, E. Troiani, G. Molinari, J. Ocaña, M. Morales, J. Porro, A. Lanciotti, V. Ristori, C. Polese, J. Plaisier, A. Lausi, Fatigue in laser shock peened open-hole thin aluminium specimens, Mater. Sci. Eng. A. 534 (2012) 573–579, https://doi.org/10.1016/j.msea.2011.12.010.
[21] M. Khomutov, P. Potapkin, V. Cheverikin, P. Petrovskiy, A. Travyanov, I. Logachev, A. Sova, I. Smurov, Effect of hot isostatic pressing on structure and properties of intermetallic NiAl–Cr–Mo alloy produced by selective laser melting, Intermetallics 120 (2020), 106766, https://doi.org/10.1016/j.intermet.2020.106766.
[22] P.J. Noell, J.M. Rodelas, Z.N. Ghanbari, C.M. Laursen, Microstructural modification of additively manufactured metals by electropulsing, Addit. Manuf. 33 (2020), 101128, https://doi.org/10.1016/j.addma.2020.101128.
[23] S. Periane, A. Duchosal, S. Vaudreuil, H. Chibane, A. Morandeau, M. Anthony Xavior, R. Leroy, Influence of heat treatment on the fatigue resistance of Inconel 718 fabricated by selective laser melting (SLM), Mater. Today Proc. 46 (2021) 7860–7865, https://doi.org/10.1016/j.matpr.2021.02.447.
[24] Q. Chao, S. Thomas, N. Birbilis, P. Cizek, P.D. Hodgson, D. Fabijanic, The effect of post-processing heat treatment on the microstructure, residual stress and mechanical properties of selective laser melted 316L stainless steel, Mater. Sci. Eng. A. 821 (2021), 141611, https://doi.org/10.1016/j.msea.2021.141611.
[25] T. Ronneberg, C.M. Davies, P.A. Hooper, Revealing relationships between porosity, microstructure and mechanical properties of laser powder bed fusion 316L stainless steel through heat treatment, Mater. Des. 189 (2020), 108481, https://doi.org/10.1016/j.matdes.2020.108481.
[26] W. Tillmann, L. Hagen, D. Stangier, N.F. Lopes Dias, J. Görtz, M.D. Kensy, Lapping and polishing of additively manufactured 316L substrates and their effects on the microstructural evolution and adhesion of PVD CrAlN coatings, Surf. Coat. Technol. 428 (2021), 127905, https://doi.org/10.1016/j.surfcoat.2021.127905.
[27] E. Liverani, S. Toschi, L. Ceschini, A. Fortunato, Effect of selective laser melting (SLM) process parameters on microstructure and mechanical properties of 316L austenitic stainless steel, J. Mater. Process. Technol. 249 (2017) 255–263, https://doi.org/10.1016/j.jmatprotec.2017.05.042.
[28] Y. Zhao, H. Xiong, X. Li, W. Qi, J. Wang, Y. Hua, T. Zhang, F. Wang, Improved corrosion performance of selective laser melted stainless steel 316L in deep sea environment, Corros. Commun. 2 (2021) 55–62, https://doi.org/10.1016/j.corcom.2021.09.002.
[29] A.A. Deev, P.A. Kuznetcov, S.N. Petrov, Anisotropy of mechanical properties and its correlation with the structure of the stainless steel 316L produced by the SLM method, Phys. Procedia 83 (2016) 789–796, https://doi.org/10.1016/j.phpro.2016.08.081.
[30] P. Bian, J. Shi, Y. Liu, Y. Xie, Influence of laser power and scanning strategy on residual stress distribution in additively manufactured 316L steel, Opt. Laser Technol. 132 (2020), 106477, https://doi.org/10.1016/j.optlastec.2020.106477.
[31] A.B. Kale, P. Alluri, A.K. Singh, S.-H. Choi, The deformation and fracture behavior of 316L SS fabricated by SLM under mini V-bending test, Int. J. Mech. Sci. 196 (2021), 106292, https://doi.org/10.1016/j.ijmecsci.2021.106292.
[32] M. Laleh, N. Haghdadi, A.E. Hughes, S. Primig, M.Y.J. Tan, Enhancing the repassivation ability and localised corrosion resistance of an additively manufactured duplex stainless steel by post-processing heat treatment, Corros. Sci. 198 (2022), 110106, https://doi.org/10.1016/j.corsci.2022.110106.
[33] M. Jaskari, J. Mäkikangas, A. Järvenpää, K. Mäntyjärvi, P. Karjalainen, Effect of High Porosity on Bending Fatigue Properties of 3D Printed AISI 316L Steel, Procedia Manuf. 36 (2019) 33–41, https://doi.org/10.1016/j.promfg.2019.08.006.
[34] G. Sander, A.P. Babu, X. Gao, D. Jiang, N. Birbilis, On the effect of build orientation and residual stress on the corrosion of 316L stainless steel prepared by selective laser melting, Corros. Sci. 179 (2021), 109149, https://doi.org/10.1016/j.corsci.2020.109149.
[35] M. Laleh, A.E. Hughes, W. Xu, I. Gibson, M.Y. Tan, Unexpected erosion-corrosion behaviour of 316L stainless steel produced by selective laser melting, Corros. Sci. 155 (2019) 67–74, https://doi.org/10.1016/j.corsci.2019.04.028.
[36] Z. Duan, C. Man, C. Dong, Z. Cui, D. Kong, L. Wang, X. Wang, Pitting behavior of SLM 316L stainless steel exposed to chloride environments with different aggressiveness: Pitting mechanism induced by gas pores, Corros. Sci. 167 (2020), 108520, https://doi.org/10.1016/j.corsci.2020.108520.
[37] G. Sander, S. Thomas, V. Cruz, M. Jurg, N. Birbilis, X. Gao, M. Brameld, C. R. Hutchinson, On the corrosion and metastable pitting characteristics of 316L stainless steel produced by selective laser melting, J. Electrochem. Soc. 164 (2017) C250–C257, https://doi.org/10.1149/2.0551706jes.
[38] G.S. Frankel, T. Li, J.R. Scully, Perspective—localized corrosion: passive film breakdown vs pit growth stability, J. Electrochem. Soc. 164 (2017) C180–C181, https://doi.org/10.1149/2.1381704jes.
[39] V. Cruz, Q. Chao, N. Birbilis, D. Fabijanic, P.D. Hodgson, S. Thomas, Electrochemical studies on the effect of residual stress on the corrosion of 316L manufactured by selective laser melting, Corros. Sci. 164 (2020), 108314, https://doi.org/10.1016/j.corsci.2019.108314.
[40] M. Laleh, A.E. Hughes, W. Xu, P. Cizek, M.Y. Tan, Unanticipated drastic decline in pitting corrosion resistance of additively manufactured 316L stainless steel after high-temperature post-processing, Corros. Sci. 165 (2020), 108412, https://doi.org/10.1016/j.corsci.2019.108412.
[41] S. Kurian, R. Mirzaeifar, Deformation mechanisms of the subgranular cellular structures in selective laser melted 316L stainless steel, Mech. Mater. 148 (2020), 103478, https://doi.org/10.1016/j.mechmat.2020.103478.
[42] C. Wang, X. Lin, L. Wang, S. Zhang, W. Huang, Cryogenic mechanical properties of 316L stainless steel fabricated by selective laser melting, Mater. Sci. Eng. A. 815 (2021), 141317, https://doi.org/10.1016/j.msea.2021.141317.
[43] C. Elangeswaran, A. Cutolo, G.K. Muralidharan, C. de Formanoir, F. Berto, K. Vanmeensel, B. Van Hooreweder, Effect of post-treatments on the fatigue behaviour of 316L stainless steel manufactured by laser powder bed fusion, Int. J. Fatigue 123 (2019) 31–39, https://doi.org/10.1016/j.ijfatigue.2019.01.013.
[44] J. Reijonen, R. Björkstrand, T. Riipinen, Z. Que, S. Metsä-Kortelainen, M. Salmi, Cross-testing laser powder bed fusion production machines and powders: Variability in mechanical properties of heat-treated 316L stainless steel, Mater. Des. 204 (2021), 109684, https://doi.org/10.1016/j.matdes.2021.109684.
[45] X. Chen, J. Li, X. Cheng, H. Wang, Z. Huang, Effect of heat treatment on microstructure, mechanical and corrosion properties of austenitic stainless steel 316L using arc additive manufacturing, Mater. Sci. Eng. A. 715 (2018) 307–314, https://doi.org/10.1016/j.msea.2017.10.002.
[46] W.-S. Shin, B. Son, W. Song, H. Sohn, H. Jang, Y.-J. Kim, C. Park, Heat treatment effect on the microstructure, mechanical properties, and wear behaviors of stainless steel 316L prepared via selective laser melting, Mater. Sci. Eng. A. 806 (2021), 140805, https://doi.org/10.1016/j.msea.2021.140805.
[47] E. Tascioglu, Y. Karabulut, Y. Kaynak, Influence of heat treatment temperature on the microstructural, mechanical, and wear behavior of 316L stainless steel fabricated by laser powder bed additive manufacturing, Int. J. Adv. Manuf. Technol. 107 (2020) 1947–1956, https://doi.org/10.1007/s00170-020-04972-0.
[48] D. Kong, X. Ni, C. Dong, L. Zhang, C. Man, J. Yao, K. Xiao, X. Li, Heat treatment effect on the microstructure and corrosion behavior of 316L stainless steel fabricated by selective laser melting for proton exchange membrane fuel cells, Electrochim. Acta 276 (2018) 293–303, https://doi.org/10.1016/j.electacta.2018.04.188.
[49] K. Wang, Q. Chao, M. Annasamy, P.D. Hodgson, S. Thomas, N. Birbilis, D. Fabijanic, On the pitting behaviour of laser powder bed fusion prepared 316L stainless steel upon post-processing heat treatments, Corros. Sci. 197 (2022), 110060, https://doi.org/10.1016/j.corsci.2021.110060.
[50] C. Wang, P. Zhu, Y.H. Lu, T. Shoji, Effect of heat treatment temperature on microstructure and tensile properties of austenitic stainless 316L using wire and arc additive manufacturing, Mater. Sci. Eng. A. 832 (2022), 142446, https://doi.org/10.1016/j.msea.2021.142446.
[51] K. Saeidi, X. Gao, F. Lofaj, L. Kvetková, Z.J. Shen, Transformation of austenite to duplex austenite-ferrite assembly in annealed stainless steel 316L consolidated by laser melting, J. Alloy. Compd. 633 (2015) 463–469, https://doi.org/10.1016/j.jallcom.2015.01.249.
[52] O.O. Salman, C. Gammer, A.K. Chaubey, J. Eckert, S. Scudino, Effect of heat treatment on microstructure and mechanical properties of 316L steel synthesized

by selective laser melting, Mater. Sci. Eng. A. 748 (2019) 205–212, https://doi.org/10.1016/j.msea.2019.01.110.
[53] M. Moyle, C. Ledermueller, Z. Zou, S. Primig, N. Haghdadi, Materials Characterization Multi-scale characterisation of microstructure and texture of 316L stainless steel manufactured by laser powder bed fusion, Mater. Charact. 184 (2022), 111663, https://doi.org/10.1016/j.matchar.2021.111663.
[54] V.B. Vukkum, R.K. Gupta, Review on corrosion performance of laser powder-bed fusion printed 316L stainless steel: Effect of processing parameters, manufacturing defects, post-processing, feedstock, and microstructure, Mater. Des. 221 (2022), 110874, https://doi.org/10.1016/j.matdes.2022.110874.
[55] Q. Chao, V. Cruz, S. Thomas, N. Birbilis, P. Collins, A. Taylor, P.D. Hodgson, D. Fabijanic, On the enhanced corrosion resistance of a selective laser melted austenitic stainless steel, Scr. Mater. 141 (2017) 94–98, https://doi.org/10.1016/j.scriptamat.2017.07.037.
[56] X. Yan, C. Shi, T. Liu, Y. Ye, C. Chang, W. Ma, C. Deng, S. Yin, H. Liao, M. Liu, Effect of heat treatment on the corrosion resistance behavior of selective laser melted Ti6Al4V ELI, Surf. Coat. Technol. 396 (2020), 125955, https://doi.org/10.1016/j.surfcoat.2020.125955.
[57] Z.J. Zheng, Y. Gao, Y. Gui, M. Zhu, Studying the fine microstructure of the passive film on nanocrystalline 304 stainless steel by EIS, XPS, and AFM, J. Solid State Electrochem. 18 (2014) 2201–2210, https://doi.org/10.1007/s10008-014-2472-5.
[58] A. Kocijan, D.K. Merl, M. Jenko, The corrosion behaviour of austenitic and duplex stainless steels in artificial saliva with the addition of fluoride, Corros. Sci. 53 (2011) 776–783, https://doi.org/10.1016/j.corsci.2010.11.010.
[59] G.J. Brug, A.L.G. van den Eeden, M. Sluyters-Rehbach, J.H. Sluyters, The analysis of electrode impedances complicated by the presence of a constant phase element, J. Electroanal. Chem. Interfacial Electrochem. 176 (1984) 275–295, https://doi.org/10.1016/S0022-0728(84)80324-1.
[60] B. Hirschorn, M.E. Orazem, B. Tribollet, V. Vivier, I. Frateur, M. Musiani, Determination of effective capacitance and film thickness from constant-phase-element parameters, Electrochim. Acta 55 (2010) 6218–6227, https://doi.org/10.1016/j.electacta.2009.10.065.
[61] M.G.S. Ferreira, M. Da Cunha Belo, N.E. Hakiki, G. Goodlet, M.F. Montemor, A.M. P. Simões, Semiconducting properties of oxide and passive films formed on AISI 304 stainless steel and Alloy 600, J. Braz. Chem. Soc. 13 (2002), https://doi.org/10.1590/S0103-50532002000400005.
[62] B. Lynch, Z. Wang, L. Ma, E.-M. Paschalidou, F. Wiame, V. Maurice, P. Marcus, Passivation-induced Cr and Mo enrichments of 316L stainless steel surfaces and effects of controlled pre-oxidation, J. Electrochem. Soc. 167 (2020), 141509, https://doi.org/10.1149/1945-7111/abc727.